



Photothermal conversion-coordinated Fenton-like and photocatalytic reactions of Cu_{2-x}Se-Au Janus nanoparticles for tri-combination antitumor therapy



Yuanlin Wang^a, Zhenglin Li^a, Ying Hu^b, Jing Liu^c, Mengyu Guo^c, Hengxiang Wei^a, Shanliang Zheng^b, Tingting Jiang^a, Xiang Sun^a, Zhuo Ma^b, Ye Sun^{d,**}, Flemming Besenbacher^e, Chunying Chen^c, Miao Yu^{a,*}

^a School of Chemistry and Chemical Engineering, Harbin Institute of Technology, Harbin, 150001, China

^b School of Life Science and Technology, Harbin Institute of Technology, Harbin, 150001, China

^c National Center for Nanoscience and Technology, Chinese Academy of Sciences, Beijing, 100190, China

^d Condensed Matter Science and Technology Institute, Harbin Institute of Technology, Harbin, 150001, China

^e Interdisciplinary Nanoscience Center (iNANO) and Department of Physics and Astronomy, Aarhus University, Aarhus, 8000, Denmark

ARTICLE INFO

Keywords:

Photothermal therapy
Chemodynamic therapy
Photocatalytic therapy
Multimodal imaging
In vivo chemical Reaction

ABSTRACT

In vivo chemical reactions activated by the tumor microenvironment (TME) are particularly promising for antitumor treatments. Herein, employing Cu_{2-x}Se-Au Janus nanoparticles (NPs), photothermal conversion-coordinated Fenton-like and photocatalytic reactions are demonstrated *in vitro/vivo*. The amorphous form of Cu_{2-x}Se and the catalytic effect of Au benefit the ·OH generation, and the photo-induced electron-hole separation of the Janus NPs produces additional ·OH. The plasmonic electrons of Au facilitate the conversion from Cu²⁺ to Cu⁺. Both Cu_{2-x}Se and Au contributes to the efficient photothermal conversion, further promoting the reactions. As a result, the H₂O₂ utilization rate is largely increased, and remarkable generation of reactive oxygen species is achieved by cell endogenous H₂O₂ *in vitro/vivo*. A competent tumor inhibition effect is afforded, with high-contrast multimodal imaging. This work opens up the route synergistically integrating photothermal therapy with chemodynamic therapy and photocatalytic therapy into tri-combination antitumor therapy, simply by heterojunction of semiconductor and noble metal.

1. Introduction

In vivo chemical reactions activated by the tumor microenvironment (TME), such as hypoxia, low pH, rich hydrogen peroxide (H₂O₂), have stimulated increased level of interest as antitumor therapies [1–4]. Chemodynamic therapy (CDT), based on the Fenton type reactions to produce hydroxyl radical (·OH), is representative [5–7]. Being the most vigorous among all reactive oxygen species (ROS), the high reactivity and short half-life of ·OH endow CDT both antitumor capability and tumor-area specificity [8–12]. Despite the major progress and promising potential of CDT, extrinsic addition of H₂O₂ was often required due to the insufficient ·OH generation by the Fenton reactions with endogenous H₂O₂ [7,13,14]. Synergistic *in vivo* chemical reactions significantly promoting ·OH generation from cell endogenous H₂O₂ are, therefore, highly preferred.

Photothermal therapy (PTT), employing photothermal agents to convert external near-infrared light (NIR) into heat and ablate tumors by hyperthermia, has become particularly fascinating in recent years [15–18]. To improve the antitumor efficacy, PTT is often integrated with chemotherapy [19,20]. Nevertheless, the high toxicity of chemotherapeutic agents and drug resistance of certain cancer cells depress the prospect [21]. An alternative combination choice is photodynamic therapy (PDT). Still, PDT cannot function synchronously with PTT as it requires a different irradiation wavelength, and the inherent hypoxia of cancer cells also restrains the PDT effect [22,23]. Incorporating with alternative non-toxic, efficient, TME-activated therapies would be desirable.

Very recently, hybrid nanoparticles integrating semiconductor with noble metal have demonstrated intriguing properties applied for antitumor therapies and photocatalysis [24–26]. In particular, combination

* Corresponding author.

** Corresponding author.

E-mail addresses: sunye@hit.edu.cn (Y. Sun), miaoyu_che@hit.edu.cn (M. Yu).

for 30 min, then mixed with CuSO_4 (2%, 5 mL) and AA (10%, 3 mL) under vigorous stirring. After reaction for 30 h, the Cu_{2-x}Se NPs were centrifuged and washed with DI water twice. Then Cu_{2-x}Se NPs was suspended in DI water (50 mL), and HAuCl_4 (2%, 2 mL) were added and reacted for 3 h to form the *c-Janus* NPs.

2.3. Sample characterization

The morphology of the sample was characterized using the transmission electron microscopy (TEM, JME-2100, JPN). The composition of the samples was analyzed by the elementary mapping using high resolution transmission electron microscopy (HR-TEM, Tecnai G20, FEI Co., USA). Sample crystallization nature was examined by X-ray diffraction (XRD) using an X-ray diffractometer (Bruker Advanced D8 Discover, USA). The optical absorption was investigated using ultraviolet–visible–near-infrared (UV–vis–NIR) spectro-photometer (Evolution 300, Thermo Scientific, USA). The fluorescence absorption was determined by using fluorescence spectrophotometer (Cary Eclipse, Varian, USA). X-ray photoelectron spectroscopy (XPS) analysis was carried out by AXIS ULTRA DLD (Kratos, UK) with an Al $K\alpha$ source. Ultraviolet–visible diffuse reflectance spectra (UV–vis DRS) were recorded on a spectrophotometer (Varian Cary 300, Agilent, CAN) from 200 to 1500 nm with BaSO_4 as the reference material. ^1H nuclear magnetic resonance (NMR) spectra were taken using an NMR spectrometer (Varian NMR System, 400 MHz). The Cu ion concentration was evaluated using an XSERIES 2 inductively coupled plasma mass spectrometer (ICP-MS).

2.4. Measurement of photothermal properties

The temperature rise of the aqueous dispersions was recorded by using a thermocouple microprobe immersed in the liquid. To evaluate the photothermal conversion efficiency (η), the sample aqueous dispersion (Cu ion concentration of $30 \mu\text{g mL}^{-1}$) was irradiated by an 808 nm laser (1.2 W cm^{-2}) until the aqueous dispersion temperature was steady, followed by cooling the dispersion temperature to ambient temperature with the laser switched off [39]. To explore the photothermal conversion stability of the $\text{Cu}_{2-x}\text{Se-Au}$ NPs, its aqueous dispersion (Cu ion concentration of $30 \mu\text{g mL}^{-1}$) was irradiated by the NIR laser (1.2 W cm^{-2}) for 5 min, then the laser was off for 5 min to cool the sample. The on/off irradiation cycle was repeated for six times.

2.5. Fenton-like and photocatalytic reactions

To assess the amount of hydroxyl radical ($\cdot\text{OH}$) generated by the Fenton-like reaction, the amorphous Janus NPs (at a Cu ion concentration of $20 \mu\text{g mL}^{-1}$) were mixed with H_2O_2 (10 mmol L^{-1}) and methylene blue (MB, $10 \mu\text{g mL}^{-1}$) in PBS buffer (pH 7.4) for 10 min at 37°C and 60°C , respectively. After centrifugation at 13,500 rpm for 10 min, the UV–vis–NIR absorbance of MB was measured. To evaluate the H_2O_2 consumption of the Fenton-like reaction, the amorphous $\text{Cu}_{2-x}\text{Se-Au}$ NPs (Cu ion concentration of $20 \mu\text{g mL}^{-1}$) were incubated with H_2O_2 (10 mmol L^{-1}) at 37°C and 60°C , respectively, for various durations. The mixture of $\text{Ti}(\text{SO}_4)_2$ was prepared by mixing $\text{Ti}(\text{SO}_4)_2$ (24%, 1.33 mL) and H_2SO_4 (8.33 mL) in DI water (40.33 mL). Following addition of the mixture (100 μL), the absorbance at 405 nm was measured to determine the concentration of H_2O_2 .

For the $\cdot\text{OH}$ generation in the Fenton-like and photocatalytic reaction, the samples (the Janus or Cu_{2-x}Se NPs, at a Cu ion concentration of $20 \mu\text{g mL}^{-1}$) were mixed with H_2O_2 (10 mmol L^{-1}) and MB ($10 \mu\text{g mL}^{-1}$) in PBS buffer (pH 7.4) and irradiated by an 808 nm laser at a power density of 1.2 W cm^{-2} for 5 min. The following measurements of MB absorbance and H_2O_2 consumption were same to those described above.

For the comparison between the amorphous $\text{Cu}_{2-x}\text{Se-Au}$ Janus and *c-Janus* NPs, the sample (Cu ion concentration of $15 \mu\text{g mL}^{-1}$) was mixed

with H_2O_2 (10 mmol L^{-1}) and MB ($10 \mu\text{g mL}^{-1}$) in PBS buffer (pH 7.4) at 60°C or irradiated by an 808 nm laser (1.0 W cm^{-2}) for 5 min. After centrifugation at 13,500 rpm for 10 min, the UV–vis–NIR absorbance of MB was measured.

2.6. Measurement of photocurrent response

The $\text{Cu}_{2-x}\text{Se-Au}$ Janus NPs and Cu_{2-x}Se NPs were respectively spin-coated on indium tin oxide (ITO) films as the working electrode in a three-electrode potentiostatic system, with Ag/AgCl (saturated 3 M KCl) as the reference electrode and Pt plate as the counter electrode. All the electrodes were immersed in 0.1 mol L^{-1} Na_2SO_4 solution. The working electrode was then irradiated by a solar simulator (0.1 W cm^{-2}) or an 808 nm laser (1.2 W cm^{-2}) for 20 s, then irradiation was off for 20 s. Five cycles of the photocurrent response were recorded.

2.7. Efficient production of Cu^+ ions from Janus NPs under irradiation

The production of Cu^+ ions by the Janus NPs under the 808 nm laser irradiation was demonstrated by Cu^+ ions catalyzed 1,3-dipolar azide-alkyne cycloaddition (CuAAC) reaction [40]. Typically, benzyl azide ($50 \mu\text{g}$) and phenylacetylene ($50 \mu\text{g}$) were added in the Janus NPs suspension (Cu ion concentration of $15 \mu\text{g mL}^{-1}$, 1 mL). The mixture was irradiated for 10 min (808 nm, 1.0 W cm^{-2}). Ethyl acetate (5 mL) was then used to extract the reactants and product (i.e. 1-benzyl-4-phenyl-1,2,3-triazole). After extraction, the ethyl acetate was removed by rotary evaporation, and the obtained substance was dissolved with deuterated chloroform and analyzed using ^1H NMR. The proton chemical shifts at 7.57 and 5.69 ppm corresponding to the formation of 1-benzyl-4-phenyl-1,2,3-triazole are characteristic for CuAAC reaction.

2.8. In vitro cytotoxicity and hemolysis assay and ROS generation

Cell counting Kit-8 (CCK-8) assay was used to assess the cytotoxicity of the Janus NPs. Human umbilical vein endothelial cell (HUVEC) and 4T1 cells purchased from Chinese Academy of Sciences Cell Bank (1.0×10^5 cells per well) were first cultured on 96-well plate over night (RPMI-1640 medium supplemented with 10% fetal bovine serum and 1% penicillin and streptomycin), then incubated with the Janus NPs dispersions at various concentrations ($0\text{--}500 \mu\text{g mL}^{-1}$) for 24 h and 48 h, respectively. HUVEC and 4T1 cells after incubation with doxorubicin hydrochloride (DOX-HCl, 98%, Aladdin, $4 \mu\text{g mL}^{-1}$) for 24 h was used as the positive control. The cells were washed with PBS for three times after incubation, then RPMI-1640 medium (100 μL) and CCK-8 (10 μL) were added to each well. One hour later, the optical absorption (at 450 nm) of each well was measured using a microplate absorbance reader (BIO-680, U.S.).

To test the hemolysis of the Janus NPs, human red blood cells (RBCs) suspension (0.1 mL) was added to 0.9 mL of DI water (positive control), PBS (negative control), and Janus NPs dispersions at various concentrations ($20\text{--}1000 \mu\text{g mL}^{-1}$), respectively. Twelve hours later, the samples were centrifuged at 15,000 rpm for 10 min. The absorbance (at 577 nm) of each sample was measured. The percentage of hemolysis was calculated following the equation: hemolysis percent (%) = $(A_s - A_n)/(A_p - A_n) \times 100\%$, where A_p , A_n , and A_s were the absorbance of the positive control, negative control and the sample groups, respectively. The morphology variation of RBCs after the treatments was characterized by SEM.

2.9. In vitro/vivo PTT–CDT–PCT therapy

To explore the PTT–CDT–PCT anticancer effect of the Janus NPs *in vitro*, HUVEC and 4T1 cells (2.5×10^5 cells per well) were incubated with the Janus NPs (in 1640 medium, $100 \mu\text{g mL}^{-1}$) on 6-well plate for 4 h, 12 h, 24 h or irradiated by the laser for 10 min (1.2 W cm^{-2}) in

presence of the Janus NPs without previous/subsequent incubation. After replacing the medium with fresh 1640 medium containing DCFH-DA ($20 \mu\text{mol L}^{-1}$, $300 \mu\text{L}$) and incubated for 30 min, the cells were rinsed and analyzed by flow cytometry, fluorescence microscope, and CCK-8 assay.

To prepare the tumor model, 1.0×10^6 4T1 cells were suspended in fresh RPMI-1640 medium ($50 \mu\text{L}$) and subcutaneously injected into the right back region of four-week-old BALB/c mice. When the tumor diameter reached about 8–10 mm, the tumor-bearing mice were divided into three groups randomly ($n = 3$, in each group), and intratumoral (i.t.) injected with PBS (Group 1) only, Janus NPs dispersion only (5 mg mL^{-1} , $50 \mu\text{L}$, Group 2), or irradiated with laser (808 nm , 0.36 W cm^{-2} , 10 min) following injection of the Janus NPs (5 mg mL^{-1} , $50 \mu\text{L}$) (Group 3), respectively. During the irradiation, the temperature of mice body was monitored by an IR thermal imager (Ti25, Fluke, USA). After the treatment, tumor size and body weight of the each mice were measured every two days. And the tumor growth inhibition rate (TGIR) was calculated according to the equation: $\text{TGIR} (\%) = (1 - G/G_0) \times 100\%$. The tissues of major organs of the mice were stained by hematoxylin and eosin (H&E) and imaged using an inverted fluorescence microscope (IX71, Olympus, Japan) for histology analysis. All animal experiments were carried out under protocols approved by the Institutional Animal Care and Use Committee. The approval number of animals is IACUC-2019021.

2.10. *In vivo* ROS generation in tumor

DHE (2 mmol L^{-1} , $20 \mu\text{L}$) was intratumorally injected to the tumor-bearing mice. Thirty minutes later, three different treatments were applied to three groups of mice: (1) Group 1, injection of PBS plus 10 min irradiation (0.6 W cm^{-2}), measured immediately after the irradiation; (2) Group 2, injection of the Janus NPs (5 mg mL^{-1} , $50 \mu\text{L}$) without irradiation, measured at 24 h after injection; (3) Group 3, injection of the Janus NPs (5 mg mL^{-1} , $50 \mu\text{L}$) injection plus 10 min irradiation (0.6 W cm^{-2}), measured immediately after the irradiation. After that, the tumors were collected and characterized using a confocal laser scanning microscopy (Zeiss LSM710).

2.11. PA/CT imaging

The PA imaging was carried out by using InVision 128 MSOT system (iThera Medical, Germany) at the excitation wavelength of 808 nm . For *in vivo* PA imaging, the NPs dispersion (2 mg mL^{-1} , $50 \mu\text{L}$) were i. t. injected to the tumor-bearing nude mice, and analyzed by using the InVision 128 MSOT system.

The CT imaging was collected by using small mice CT (80 mA , 100 kV , slice thickness of 0.625 mm). For *in vivo* CT experiments, the Janus NPs dispersion (10 mg mL^{-1} , $50 \mu\text{L}$) was i. t. injected to the tumor-bearing nude mice. Twenty minutes later, the mice were anesthetized and imaged. The images were analyzed using amira 4.1.2.

2.12. Statistical analysis

The experimental data were analyzed by two-tailed Student's *t*-test, given the small sample number ($n = 3$). $*p \leq 0.05$ and $**p \leq 0.01$ were considered to be statistically significant.

3. Results and discussion

3.1. Synthesis, characterization and photothermal conversion of $\text{Cu}_{2-x}\text{Se-Au}$ NPs

The $\text{Cu}_{2-x}\text{Se-Au}$ NPs were synthesized by a facile oxidation-reduction method. The transmission electron microscopy (TEM) images (Fig. 1a–b) revealed that the NPs were monodispersed, showing a distinct Janus form with a size of $30.4 \pm 2.5 \text{ nm}$ (where the size of the Au

core was $14.4 \pm 1.4 \text{ nm}$). According to the elemental mapping (Fig. 1c), the dark circular and light half-moon portion of each NP were attributed to the Au core and Cu_{2-x}Se semi-enclosed shell, respectively. Based on the analysis using energy dispersive spectroscopy (EDS, Fig. S1 and Table S1), the ratio of Cu/Se was 1.2:1. The X-ray diffraction (XRD) pattern (Fig. S2) showed that the Au core was highly crystalline whilst the Cu_{2-x}Se was amorphous. The monodispersity and good water solubility of the Janus NPs were confirmed by the linearly increased optical absorbance with the dispersion concentration in water (Fig. S3) and the dynamic light scattering (DLS) results (Fig. S4). The optical absorption property of the Janus NPs was distinct from that of either the Au or Cu_{2-x}Se NPs alone (Fig. 1d and Fig. S5), showing a strong and broad absorption in the NIR region, besides the evident peak located at $\sim 635 \text{ nm}$. Such modification is attributed to the coating of Cu_{2-x}Se on the Au core and the varied band structure (Fig. S6) of the Janus NPs due to the $\text{Cu}_{2-x}\text{Se-Au}$ coupling.

We then explored the photothermal property of the Janus NPs. The dispersion temperature showed sensitive response to the irradiation, following a concentration- and irradiation duration-dependent fashion (Fig. 1e). For instance, a large temperature elevation from $\sim 29.2 \text{ }^\circ\text{C}$ to $\sim 76.2 \text{ }^\circ\text{C}$ was achieved upon 8 min irradiation (Cu ion concentration of $30 \mu\text{g mL}^{-1}$, 808 nm , 1.2 W cm^{-2}); whilst the temperature of the control group, i.e. deionized (DI) water, was barely varied ($\Delta T = 1.6 \text{ }^\circ\text{C}$) under the same irradiation conditions. The photothermal conversion efficiency (η) of the Janus NPs was calculated from the heating and cooling curves (Fig. S7a–b and Table S2), deducing an efficiency as high as $\sim 67.2\%$, higher than that of the Cu_{2-x}Se nanocrystals (22%), nanostructured Au particles (21%), or $\text{Au@Cu}_{2-x}\text{S}$ NPs (52.1%) reported previously [24,29,41]. Besides, the Janus NPs also possessed reliable photothermal conversion stability, as evidenced by the reproducible temperature elevation upon the six irradiation cycles (Fig. 1f). No noticeable variation was observed from the optical absorption spectrum after the cycling (Fig. S7d), indicating the good photothermal stability of the Janus NPs.

To figure out the role of the Au core in photothermal conversion, the optical absorption and photothermal conversion capability of the Janus NPs were compared with those of pure Cu_{2-x}Se NPs synthesized using the same method as the Cu_{2-x}Se semi-enclosed shell in the Janus NP. Although Au barely contributed any optical absorbance at 808 nm , the absorbance of the Janus NPs was evidently higher than that of Cu_{2-x}Se at the identical Cu concentration ($30 \mu\text{g mL}^{-1}$) (Fig. S5). Moreover, by tuning the concentration of the Janus and Cu_{2-x}Se dispersion to get them reach the same absorbance at 808 nm (Fig. S8a–b), larger temperature elevation was achieved from the Janus NPs dispersion upon the same irradiation, pointing out the higher photothermal conversion capability of the Janus NPs. Consistently, although the Au core alone showed nearly no temperature variation upon the 808 nm irradiation, the dispersion temperature of the Janus NPs was much higher than that of Cu_{2-x}Se at each given dispersion concentration (Fig. 1e vs. Fig. S8).

3.2. Fenton-like and photocatalytic reactions with H_2O_2

The $\cdot\text{OH}$ generation and H_2O_2 consumption mediated by the Janus NPs were investigated using the methylene blue (MB) probing technique and $\text{Ti}(\text{SO}_4)_2$ solution, respectively. Since $\cdot\text{OH}$ is capable to bleach MB efficiently, the $\cdot\text{OH}$ generation can be evaluated by the optical absorption decrease of MB [5]. The Janus NPs (Cu ion concentration as low as $20 \mu\text{g mL}^{-1}$) was found to be able to react with H_2O_2 under different conditions. Both the $\cdot\text{OH}$ generation and H_2O_2 consumption followed a temperature-sensitive manner (Fig. 2a–b). Clearly, much more efficient $\cdot\text{OH}$ generation was achieved upon the NIR irradiation. Irradiation at 1.2 W cm^{-2} for 5 min (corresponding to a temperature rise process from $30.0 \text{ }^\circ\text{C}$ to $60.0 \text{ }^\circ\text{C}$) can already bleach $\sim 99.5\%$ of MB; whilst keeping the solution at $60.0 \text{ }^\circ\text{C}$ (without irradiation) even for 10 min, the MB peak was only reduced by $\sim 85.2\%$. Very interestingly, under the same irradiation power density and

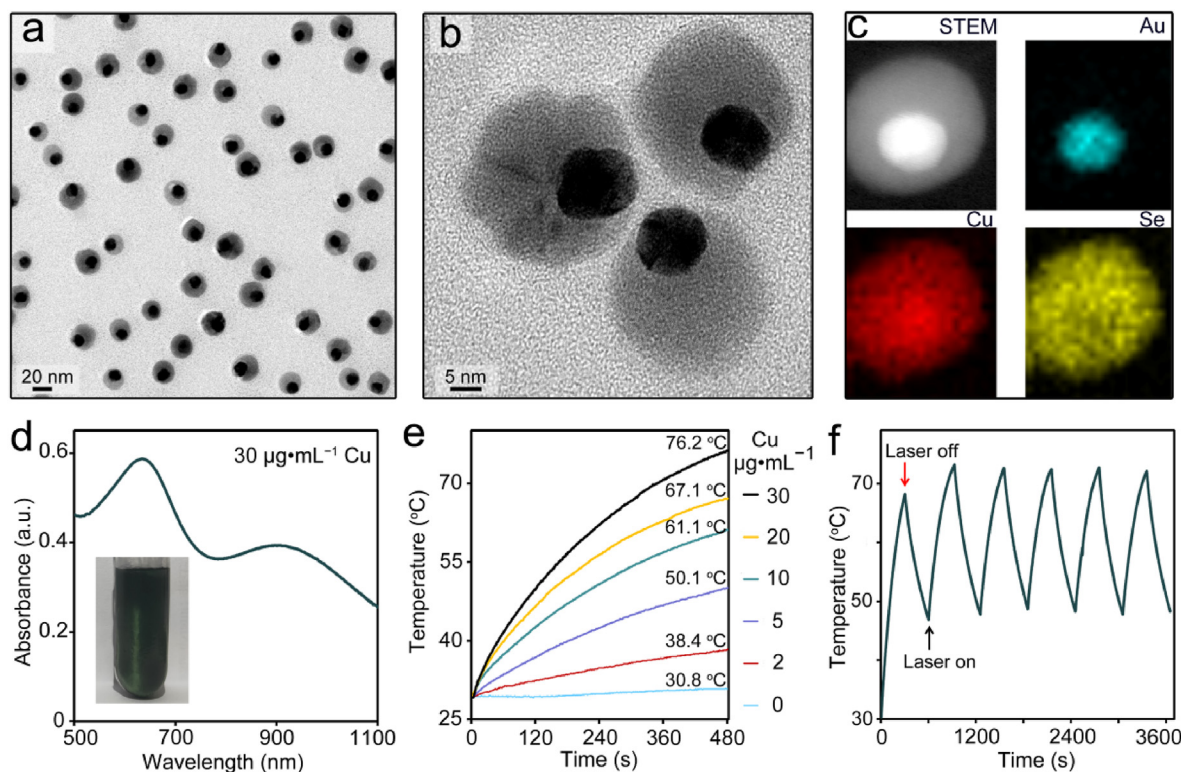


Fig. 1. Morphology, composition, optical absorption and photothermal conversion of the $\text{Cu}_{2-x}\text{Se-Au}$ Janus NPs. (a–b) TEM images at different scales, showing dispersed, uniform NPs with a typical Janus morphology. (c) Elemental mapping of an individual Janus NP, showing the presence and distribution of Au, Cu and Se. (d) UV–vis–NIR absorption spectrum and a digital photo of the Janus NPs dispersion at a Cu ion concentration of $30 \mu\text{g mL}^{-1}$. (e) Temperature elevation of the Janus NPs at various concentrations upon 808 nm irradiation (1.2 W cm^{-2}). (f) Temperature elevation curve mediated by the Janus NPs upon repeated irradiation cycles.

duration, although the $\cdot\text{OH}$ generation rate (r_G , determined by the MB peak decrease rate) of the Janus NPs was significantly elevated compared with that of the Cu_{2-x}Se , the H_2O_2 consumption rate (r_C) of the former was much lower (Fig. 2c–d). As a result, the H_2O_2 utilization efficiency ($\eta_U = r_G/r_C$) mediated by the Janus NPs was ~ 3.65 and 5.38 folds as that of the Cu_{2-x}Se under an irradiation of 0.8 W cm^{-2} and 1.2 W cm^{-2} , respectively. Especially, upon 5 min irradiation, the sample solution temperature increased by the Janus NPs irradiated at 0.8 W cm^{-2} ($\sim 51^\circ\text{C}$) was nearly identical to the temperature mediated by the Cu_{2-x}Se irradiated at 1.2 W cm^{-2} , and the η_U of the Janus NPs irradiated at 0.8 W cm^{-2} was $\sim 512\%$ as that of Cu_{2-x}Se at 1.2 W cm^{-2} . All these results suggest that the Janus NPs have much powerful $\cdot\text{OH}$ generation capability and higher H_2O_2 utilization rate than Cu_{2-x}Se alone.

Furthermore, we compared the $\cdot\text{OH}$ generation of our Janus NPs with another $\text{Cu}_{2-x}\text{Se-Au}$ hybrid particles where the Cu_{2-x}Se semi-sphere is in a high crystalline form (*c-Janus*). It was found that, no matter keeping at 60°C or irradiated for 5 min (808 nm , 1.0 W cm^{-2}), the $\cdot\text{OH}$ generation mediated by the amorphous $\text{Cu}_{2-x}\text{Se-Au}$ NPs was always higher than that by *c-Janus*. As shown in Fig. S9, the MB degradation rate mediated by the amorphous Janus NPs is $\sim 44.9\%$ and 87.1% at 60°C and under 5 min 808 nm irradiation, which is evidently higher than that of *c-Janus* ($\sim 33.5\%$ at 60°C and $\sim 26.3\%$ under 5 min irradiation). The $\cdot\text{OH}$ generation of the amorphous Janus sample was ~ 3.3 fold as that of *c-Janus* under the 5 min irradiation (Cu ion concentration of $15 \mu\text{g mL}^{-1}$). The results indicate that the amorphous feature of Cu_{2-x}Se is beneficial for the $\cdot\text{OH}$ generation of the Janus NPs. This is very likely the reason that CDT of hybrid copper oxides/chalcogenide-Au NPs has not been reported previously.

3.3. Mechanisms for the promoted photothermal conversion and chemical reactions

As mentioned above, the enhanced photothermal properties of Janus NPs were reflected not only in the higher optical absorption at 808 nm , but also in the enhanced photothermal conversion capability. Compared with the optical absorption spectrum of the Cu_{2-x}Se NPs (Fig. 1d and Fig. S5), the large red-shift of the absorption peak from 515 nm to 635 nm and elevated absorbance in the NIR region both suggest the strong coupling between the Au core and the Cu_{2-x}Se semi-enclosed shell in the Janus NP. Similar to the reported $\text{Au@Cu}_{2-x}\text{S}$ NPs [24,42], such coupling and the absorption at 808 nm of the Janus NPs can enable the LSPR of Au NPs and effectively arouse the photothermal effect.

Importantly, significant photocurrent response of the Janus NPs was evidenced under both solar irradiation (Figs. 2e., 0.1 W cm^{-2}) and 808 nm laser (Figs. 2f., 1.2 W cm^{-2}), whilst the response of Cu_{2-x}Se alone in both cases was rather weak. The results indicate the efficient electron–hole separation of Cu_{2-x}Se in the presence of Au core, further confirming the strong Au– Cu_{2-x}Se coupling. Considering the much lower Fermi energy of Au than the valence band of Cu_{2-x}Se [26,43], the electron–hole separation then suggest the transfer of photo-induced electrons from the Cu_{2-x}Se shell to the Au core. Although the electron–hole separation partially may reduce the non-radiative electron–hole recombination for the photothermal conversion of the Cu_{2-x}Se , judged by the efficient temperature rise mediated by the Janus NPs as compared with the case of Cu_{2-x}Se , the transferred electrons from Cu_{2-x}Se to Au core and the LSPR effect of the Au core can remedy and promote the photothermal properties of the hybrid NPs. Especially, the unique semi-enclosed Janus form benefits not only the charge transfer from Cu_{2-x}Se to Au but also sufficient exposure of both Cu_{2-x}Se and Au to the surrounding for transfer of holes, electrons and heat.

Besides the amorphous feature of Cu_{2-x}Se mentioned above, the

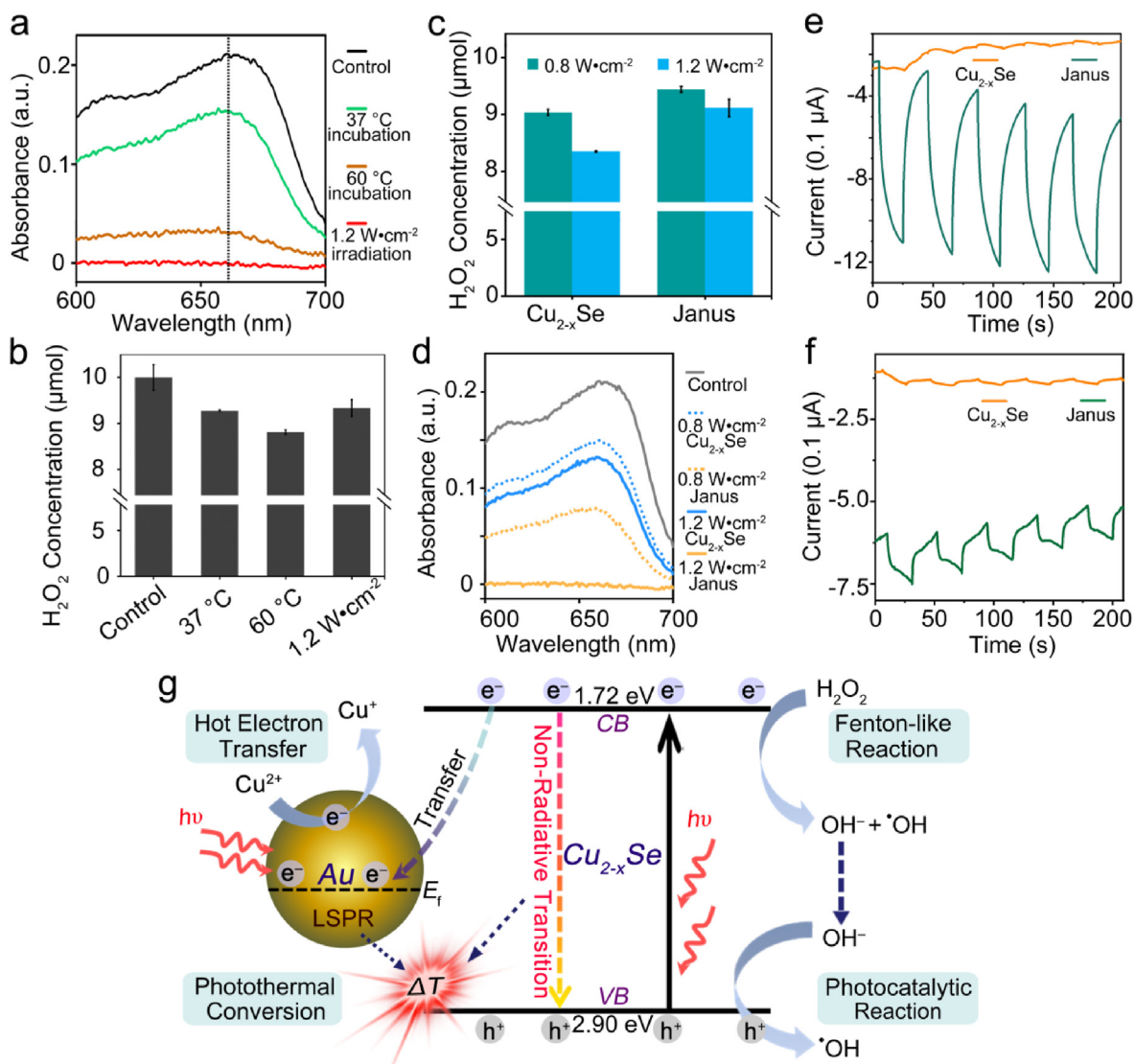


Fig. 2. Fenton-like and photocatalytic reactions mediated by the Janus NPs. (a) MB degradation induced by the Fenton-like reaction of the Janus NPs at 37 °C, 60 °C without irradiation, or under 808 nm irradiation (1.2 W cm^{-2}) for 5 min. (b) H_2O_2 consumption of the Janus NPs upon different treatments based on colorimetric analysis. (c) H_2O_2 consumption and (d) MB degradation mediated by the Janus and Cu_{2-x}Se NPs under NIR irradiation of different power densities. (e) The photocurrent response plots of the Janus and Cu_{2-x}Se NPs upon five repeated irradiation cycles under solar light of 0.1 W cm^{-2} , and (f) 808 nm laser of 1.2 W cm^{-2} . (g) Schematic illustration for the photothermal conversion-coordinated Fenton-like and photocatalytic reactions of the Janus NPs. Data in panel b and c are expressed as the mean \pm standard deviation.

efficient $\cdot\text{OH}$ generation of the Janus NPs is also associated with the catalytic effect from the Au core, the photocatalytic effect by electron-hole separation, and the photothermal conversion effect of both Au and Cu_{2-x}Se . As shown in Fig. S10, without irradiation, the participation of the Au core can catalyze the Fenton-like reaction. It has been demonstrated that supported Au can flip between the positive and neutral states to catalyze Fenton reaction [44]. Moreover, as photo-generated holes can react with OH^- to form $\cdot\text{OH}$ [45,46], in addition to the $\cdot\text{OH}$ generated by the Fenton-like reaction of Cu_{2-x}Se with H_2O_2 , i.e. $\text{Cu}^+ + \text{H}_2\text{O}_2 \rightarrow \text{Cu}^{2+} + \cdot\text{OH} + \text{OH}^-$, the Janus NPs can produce additional $\cdot\text{OH}$ from OH^- with the photo-induced holes (Fig. 2g). Such photocatalytic process is distinct from the reported anticancer PDT work utilizing the photo-generated electrons from nano-photocatalysts to produce singlet O_2 for tumor inhibition [47], and $\cdot\text{OH}$ is far more reactive and powerful than singlet O_2 in this regard. Meanwhile, the excellent photothermal property of the Janus NPs further boosts the Fenton-like and photocatalytic reactions upon the NIR irradiation [48,49], further increasing $\cdot\text{OH}$ generation.

The promoted H_2O_2 utilization rate is closely related to the different

reduction path of Cu ions. For the case of Cu_{2-x}Se alone, H_2O_2 were consumed by not only the Fenton-like reaction for $\cdot\text{OH}$ generation but also the reduction of Cu^{2+} ($\text{Cu}^{2+} + \text{H}_2\text{O}_2 \rightarrow \text{Cu}^+ + \text{O}_2\cdot^- + 2\text{H}^+$). However, for the Janus NPs, efficient production of Cu^+ ions can be achieved under irradiation, as revealed by the Cu^+ ions catalyzed 1,3-dipolar azide-alkyne cycloaddition (CuAAC) reaction (^1H nuclear magnetic resonance spectra in (Fig. S11)), where the plasmonic electrons of Au NPs are known to induce the ion reduction [50]. The presence of Au core in the Janus NPs thus effectively decreases the H_2O_2 consumption.

3.4. Biocompatibility of the Janus NPs and their high specificity of cytotoxicity on cancer cells

To explore the cytotoxicity of the Janus NPs, HUVEC (normal cell) and 4T1 cells (cancer cell) were incubated with the NPs for 24 h and 48 h, respectively. Based on the CCK-8 assay, the viability of HUVEC cells was $> 80\%$ after 24/48 h incubation (Fig. 3a and Fig. S12). In sharp contrast, the cell viability of 4T1 cells was reduced to as low as

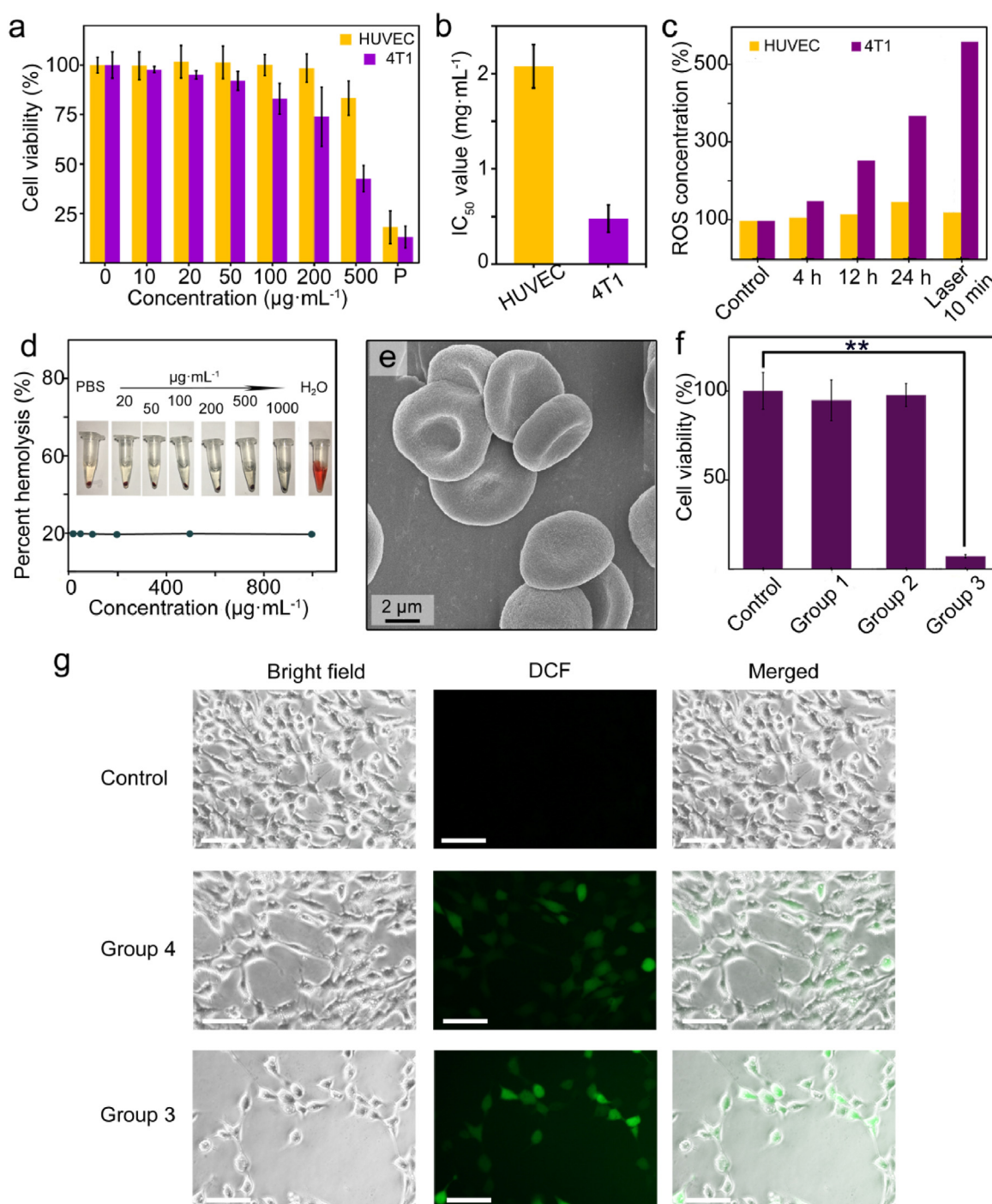


Fig. 3. The cytotoxicity and hemolytic effect of the Janus NPs. (a) Cell viability and (b) IC_{50} value of 4T1 and HUVEC cells after 24 h incubation with the Janus NPs, where cells treated by doxorubicin ($4 \mu\text{g mL}^{-1}$) is used as the positive control (P). (c) DCFH-DA stained 4T1 and HUVEC cells upon different treatments with the Janus NPs ($100 \mu\text{g mL}^{-1}$). (d) Hemolytic effect of RBCs after 24 h incubation with the Janus NPs dispersion at various concentrations, PBS (negative control), and DI water (positive control) at 37°C . (e) SEM image of RBCs treated with the Janus NPs dispersion. (f) Cell viability of the 4T1 cells treated with NIR irradiation only (Group 1), the Janus NPs only (Group 2), and the combination of Janus NPs with 10-min irradiation (Group 3). ($n = 3$, $**p \leq 0.01$). (g) Fluorescence images of DCFH-DA stained 4T1 cells after various treatments (scale bar: $25 \mu\text{m}$). Data in panel a, b and f are expressed as the mean \pm standard deviation.

$\sim 42.6\%$ under the same conditions. Half-maximum inhibitory concentration (IC_{50}) was calculated according to the cell viability (Figs. 3b and 24 h incubation), deducing a IC_{50} value of $2076.8 \mu\text{g mL}^{-1}$ and $477.6 \mu\text{g mL}^{-1}$ for the HUVEC and 4T1 cells, respectively. All the results indicate that the Janus NPs are compatible with the normal cells, but toxic to the 4T1 cells. The specificity of cytotoxicity on cancer cells is closely related to the significantly higher concentration of H_2O_2 [40,51] hence higher ROS level generated by the Janus NPs in the

cancer cells. This point was confirmed by evaluating the ROS level *in vitro* using 2',7'-dichlorofluorescent yellow diacetate (DCFH-DA) assay (Fig. 3c and Figs. S13–14). Excitingly, without extrinsic addition of H_2O_2 , notable ROS can be already generated based on the endogenous H_2O_2 of the cells. For instance, after 24 h incubation with the Janus NPs ($100 \mu\text{g mL}^{-1}$), the ROS level in the 4T1 cells increased to $\sim 371.2\%$, whilst that in the HUVEC cells was only $\sim 48.1\%$ higher. In addition, the hemolytic effect of the Janus NPs on human red blood cells (RBCs)

was also investigated. No detectable hemolysis and noticeable variation were observed in our experiments (Fig. 3d–e and Fig. S15).

To assess the anticancer efficacy of the combined PTT–CDT–PCT *in vitro*, the 4T1 cells were divided into four different groups: (1) Group 1, irradiation only (808 nm, 1.2 W cm⁻², 10 min), (2) Group 2, Janus NPs only (10 min incubation with Janus NPs at 100 µg mL⁻¹), (3) Group 3, Janus NPs (100 µg mL⁻¹) with irradiation (808 nm, 1.2 W cm⁻², 10 min), and (4) Control, treated with PBS only. Calcein acetoxyethyl ester (Calcein AM) and propidium iodide (PI) were used to stain the cells in order to distinguish the live (green) and dead (red) cells. Compared with the Control, Group 1 and 2 appeared no obvious difference, showing green fluorescence signal only (Fig. S16). The results suggest that a short incubation with the NPs or NIR irradiation alone cannot compromise the cell viability. As a sharp contrast, significant red fluorescence signal was exclusively presented in Group 3, suggesting the effective cancer cell killing. Measurements using the CCK-8 assay (Fig. 3f) further revealed that ~92.8% of the 4T1 cells were killed in Group 3, whilst other groups showed high cell viability (> 92.5%). Consistently, after DCFH-DA staining and without addition of H₂O₂, no fluorescence signal (*i.e.* sign of ROS generation) was observed in the Control group, whilst strong green fluorescence of ROS in the cells was evidenced from both Group 3 and the cells after 12 h-incubation with the Janus NPs (100 µg mL⁻¹) at 37 °C (Group 4), with the signal of Group 3 more pronounced (Fig. 3g). The ROS generated in the 4T1 cells for Group 3 was as high as ~574.2% of the Control group (Fig. 3c and Fig. S17). All these results emphasize the significant ROS generation capability and anticancer efficacy of the Janus NPs.

The ROS generation capability of the Janus NPs was further compared with that of MB, a widely-used photosensitizer for antitumor PDT treatment [52,53]. As shown in Fig. S18, MB can also improve the ROS level in 4T1 cells (~157.4%) under 670 nm irradiation (0.75 W cm⁻², 10 min), but its efficacy was far less than that of the Janus NPs. Moreover, the ROS level generated by MB in the normal cells was as high as ~30.91 folds higher than that in the cancer cells (Fig. S19). This is primarily attributed to the fact that the ROS generation by MB is based on its reaction with O₂, which is more abundant in the normal cells than that in the cancer cells. Superior to the photosensitizer in PDT, the high specific toxicity of the Janus NPs on cancer cells affords great promise on practical medical applications, besides their high anticancer efficacy.

3.5. Tumor inhibition effect of the combined PTT–CDT–PCT therapy *in vitro*

Encouraged by the promising performance *in vitro*, the antitumor therapeutic efficacy of the Janus NPs was then evaluated *in vivo*. Tumour-bearing BALB/c mice were divided randomly into three groups, including (1) PBS injection plus irradiation (Group 1), (2) Janus NPs injection only (Group 2), and (3) Janus NPs injection plus irradiation (Group 3). After intratumoral (*i.t.*) injection, the tumour area of each mouse in Group 1 and 3 was irradiated by the 808 nm laser (0.36 W·cm⁻²), and the body temperature was monitored by the real-time infrared thermal imaging. Upon 10 min irradiation, while the whole body colour was barely varied for Group 1 ($\Delta T = 2.8$ °C), the tumour area of mice in Group 3 rapidly turned red and bright, reaching a plateau of ~54 °C (Fig. 4a–b). According to the literature [54], this temperature is sufficient to induce hyperthermia for tumour inhibition. Meanwhile, the results also demonstrated the high-contrast infrared thermal imaging capability of the Janus NPs *in vivo*.

To illustrate the ROS generation and its impact on the tumour *in vivo*, tumor tissue of the three sample groups was collected 24 h after the injection and stained by dihydroethidium (DHE) and hematoxylin and eosin (H&E), respectively. As shown in Fig. 4c, unlike Group 1 which showed neither detectable tumor tissue damage nor fluorescence signal corresponding to ROS, both Group 2 and 3 exhibited obvious cell death and ROS. Especially, for the treated tumor tissue of Group 3,

significant cell variations, such as loss of contact, nuclear damage, and cell shrinkage, were observed, together with the rather bright ROS signal. The results indicate that, integrated with PTT, the ROS generated from endogenous H₂O₂ by the Fenton-like and photocatalytic reactions of the Janus NPs was abundant to achieve a significant anti-tumor effect.

The rest mice of each group after the treatments were carefully monitored. The tumor volume was measured and recorded with time (Fig. 4d). Twelve days after the treatments, each tumor was collected and weighted (Fig. 4e–g). For Group 1, despite the irradiation applied, the tumor grew rather rapidly with time. As comparison, although the tumor size of Group 2 did not obviously decrease after the NPs injection, the tumor growth rate was far less than that of Group 1, with an inhibition ratio of ~62.1%, indicating that CDT of the Janus NPs alone can already induce evident inhibition effect. Distinct from these two groups, the tumors were eliminated by the treatment of Group 3, and showed barely any recurrence in the twelve days, resulting in a high inhibition ratio of ~95.7%. The results further confirmed the competent antitumor capability of the synergistic PTT–CDT–PCT mediated by the Janus NPs *in vivo*.

Moreover, the behavior and body weight (Fig. 4h) of all treated mice were compared with the healthy mice, showing no noticeable difference. Their major organs were collected for histology analysis after H&E staining. Neither noticeable inflammation nor organ damage was visualized in all cases (Fig. 4i). These results demonstrated the no/low *in vivo* toxicity of the Janus NPs to mice.

3.6. *In vitro* and *in vivo* PA and CT imaging

The PA imaging capability of the Janus NPs was first measured *in vitro*. The PA images became gradually brighter with the NPs concentration (Fig. 5a), and the plot of signal intensity as a function of the NPs concentration showed a linear relationship (Fig. 5b). The *in vivo* PA imaging was then performed after *i.t.* injection of the Janus NPs to tumor-bearing BALB/c mice. Due to the pronounced photothermal conversion effect mediated by the NPs upon NIR irradiation, thermal expansion hence acoustic signal can be detected from the tumor area. As a result, whilst no signal was presented before injection, significant PA signal was seen in the tumor area (Fig. 5c), confirming the high-contrast PA imaging capability of the Janus NPs.

The CT imaging capacity of the Janus NPs was also evaluated. Due to the high Z (79) and high X-ray attenuation coefficient (5.16 at 100 keV) of Au [24,32,33], the Janus NPs showed strong X-ray attenuation effect, with the CT values and imaging brightness progressively increased with the NPs concentration (Fig. 5d–e). According to the measured CT values at various NPs concentrations, the CT contrast-enhancement efficiency of the Janus NPs was deduced to be 19.1 HU·mL·mg⁻¹, which was higher than that of the clinically-used CT agent (iohexol, 16.4 HU·mL·mg⁻¹). After injection, the anesthetized tumor-bearing mice were imaged by CT imaging system (Fig. 5f). Unlike the image prior to the injection where only bone structure presented, thanks to the X-ray attenuation effect of the Janus NPs, strong CT contrast signal of the tumor was clearly observed after injection.

Considering that *i.t.* injection was applied, to allow a relatively even distribution of the NPs in the tumor area, both PA and CT imaging was carried out 20 min after the injection. Still, the CT/PA images might not be able to show the exact/complete size/appearance of the tumor. However, as demonstration experiments, the high contrast imaging results confirm the potential of these Janus NPs for PA/CT imaging clearly.

4. Conclusion

In summary, We have developed Cu_{2-x}Se-Au hybrid NPs in a uniform Janus form with PTT–CDT–PCT tri-combination therapeutic modal and CT/PA/infrared thermal imaging for antitumor treatments.

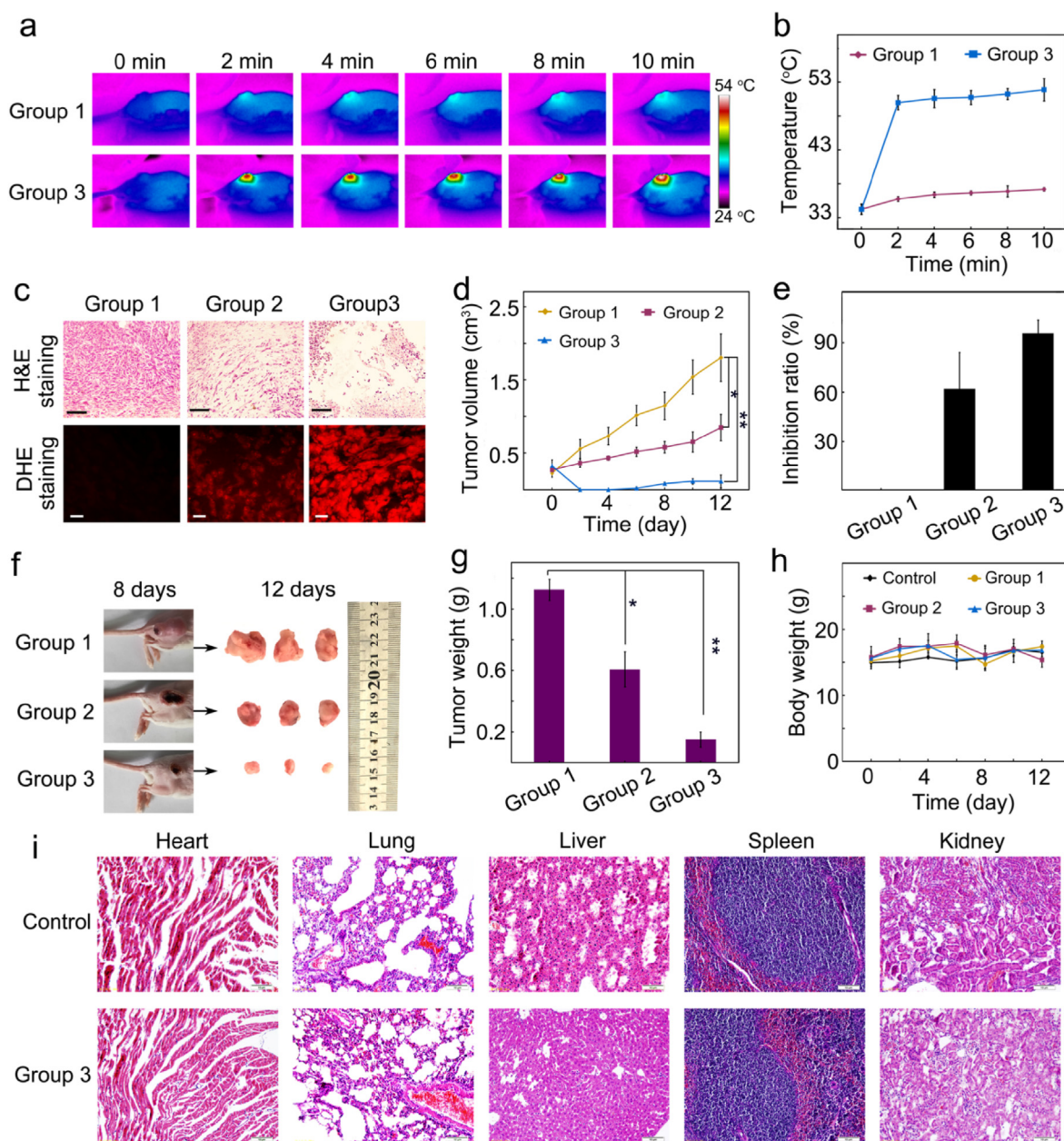


Fig. 4. *In vivo* antitumor efficacy of the Janus NPs. (a) IR thermal images of tumor-bearing mice recorded upon NIR irradiation. (b) Temperature elevation of the tumor area of Group 1 and 3 under irradiation. (c) H&E and DHE stained tumor tissue (scale bar: 100 μ m), (d) tumor volume growth curves ($n = 3$, $*p \leq 0.05$, $**p \leq 0.01$), and (e) tumor growth inhibition ratio of the treated mice in different groups. (f) The photos and (g) mean weight of the tumors collected from the mice 12 days after the various treatments ($n = 3$, $*p \leq 0.05$, $**p \leq 0.01$). (h) Body weight of mice in different groups with time ($n = 3$). (i) Histology analysis of the major organs collected from the healthy mice and Group 3. Data in panel b, d, e, g and h are expressed as the mean \pm standard deviation.

Thanks to the coupling of semiconducting Cu_{2-x}Se semi-closed shell and metallic Au core, the Janus NPs possess strong NIR absorption and high photothermal conversion capability. The amorphous morphology of Cu_{2-x}Se and the catalytic effect of the Au core enhance $\cdot\text{OH}$ generation in Fenton-like reaction; meanwhile, the efficient electron-hole separation produces additional $\cdot\text{OH}$ by the photocatalytic process. Both the reactions are further boosted by the photothermal effect. In this case, the LSPR effect of Au contributes not only to the photothermal conversion of the Janus NPs, but also to $\text{Cu}^{2+} \rightarrow \text{Cu}^{+}$ conversion, thus significantly increases utilization rate of H_2O_2 . Therefore, the simple semiconductor-noble metal hybrid not only integrates PTT with CDT and PCT into a new tri-combination antitumor therapy, but also enables remarkable ROS generation by cell endogenous H_2O_2 . As a result, the Janus NPs afford competent photothermal conversion (efficiency of

$\sim 67.2\%$) and $\cdot\text{OH}$ generation without exotic H_2O_2 , inducing a tumor inhibition rate of $\sim 95.7\%$ together with high-contrast CT/PA/infrared thermal imaging performance.

Comparing with the CDT alone and PTT-CDT reported previously, this PTT-CDT-PCT tri-combination is capable of producing sufficient $\cdot\text{OH}$ without extrinsic addition of H_2O_2 , meanwhile avoids the hazard induced by the toxicity and drug resistance of chemotherapeutic agents. Also unlike PDT that is largely confined by the inherent hypoxia of cancer cell and requires a much shorter irradiation wavelength different from that for PTT, our tri-combination therapy has specificity of cytotoxicity on cancer cells and allows the operation using single wavelength irradiation in NIR region. It is known that NIR irradiation induces much better penetration to biotic tissues than ultraviolet or visible light. As the passive accumulation of the Janus NPs based on the

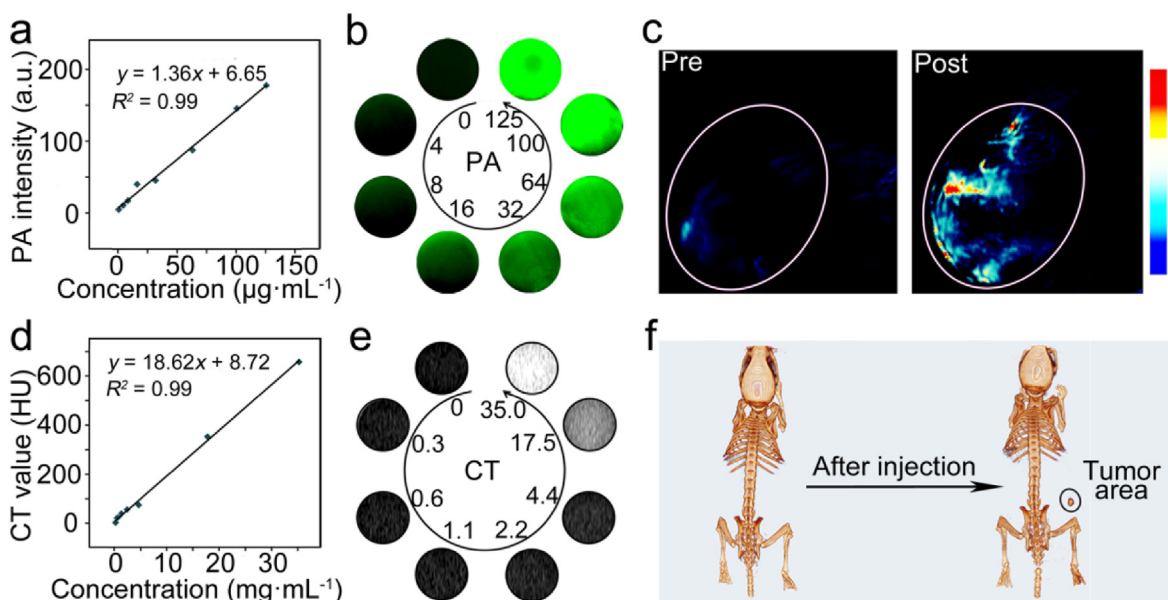


Fig. 5. *In vitro* and *in vivo* PA and CT imaging of the Janus NPs. (a) *In vitro* PA signal intensity and (b) PA images of the $\text{Cu}_{2-x}\text{Se-Au}$ Janus NPs at various concentrations. (c) PA images of tumor before (Pre) and after (Post) injection, where the tumor area is marked by a circle. (d) *In vitro* CT values and (e) CT images of the Janus NPs at various concentrations. (f) *In vivo* three-dimensional CT images of tumor-bearing mice before (Pre) and after (Post) injection.

enhanced permeability and retention effect upon intravenous injection is not significant, a proper surface modification using tumor-targeting molecules would be highly preferred to improve its application prospects. Still, such non-toxic, efficient PTT-CDT-PCT synergistic therapy based on TME-activated *in situ* chemical reactions may have opens up a fresh route for antitumor treatment. In addition, such metal-semiconductor heterojunction also holds promise on photocatalysis and other relevant combined reactions under NIR irradiation.

Data availability

The authors declare that all data supporting the findings of this study are available within the paper [and its supplementary information files]. Correspondence and requests for materials should be addressed to M. Y. or Y-S.

CRedit authorship contribution statement

Yuanlin Wang: Formal analysis, Investigation, Writing - original draft. **Zhenglin Li:** Investigation. **Ying Hu:** Methodology. **Jing Liu:** Investigation. **Mengyu Guo:** Investigation. **Hengxiang Wei:** Investigation. **Shanliang Zheng:** Investigation. **Tingting Jiang:** Investigation. **Xiang Sun:** Investigation. **Zhuo Ma:** Methodology. **Ye Sun:** Funding acquisition, Writing - review & editing. **Flemming Besenbacher:** Supervision. **Chunying Chen:** Supervision, Methodology. **Miao Yu:** Conceptualization, Funding acquisition, Writing - original draft.

Declaration of competing interest

We declare that there are no real or potential conflicts of interest associated with the present manuscript entitled '**Photothermal Conversion- Coordinated Fenton-Like and Photocatalytic Reactions of $\text{Cu}_{2-x}\text{Se-Au}$ Janus Nanoparticles for Tri-combination Antitumor Therapy**'. There has been no personal/financial interest or belief that could have inappropriately influenced the present results.

Acknowledgments

This work was financially supported by the National Natural Science Foundation of China (21473045, 51772066), and State Key Laboratory of Urban Water Resource and Environment (2018DX04).

Appendix A. Supplementary data

Supplementary data to this article can be found online at <https://doi.org/10.1016/j.biomaterials.2020.120167>.

References

- [1] C. Chang, J. Qiu, D. O'Sullivan, M.D. Buck, T. Noguchi, J.D. Curtis, Q. Chen, M. Gindin, M.M. Gubin, G.J. van der Windt, Metabolic competition in the tumor microenvironment is a driver of cancer progression, *Cell* 162 (2015) 1229–1241.
- [2] M. Chung, H. Liu, K. Lin, W.T. Chia, H.W. Sung, A pH-responsive carrier system that generates NO bubbles to trigger drug release and reverse P-glycoprotein-mediated multidrug resistance, *Angew. Chem. Int. Ed.* 54 (2015) 9890–9893.
- [3] Q. Chen, C. Liang, X. Sun, J. Chen, Z. Yang, H. Zhao, L. Feng, Z. Liu, H_2O_2 -responsive liposomal nanoprobes for photoacoustic inflammation imaging and tumor theranostics via *in vivo* chromogenic assay, *Proc. Natl. Acad. Sci. U.S.A.* 114 (2017) 5343–5348.
- [4] C. Zhang, D. Ni, Y. Liu, H. Yao, W. Bu, J. Shi, Magnesium silicide nanoparticles as a deoxygenation agent for cancer starvation therapy, *Nat. Nanotechnol.* 12 (2017) 378.
- [5] L. Lin, J. Song, L. Song, K. Ke, Y. Liu, Z. Zhou, Z. Shen, J. Li, Z. Yang, W. Tang, Simultaneous fenton-like ion delivery and glutathione depletion by MnO_2 -based nanoagent to enhance chemodynamic therapy, *Angew. Chem. Int. Ed.* 57 (2018) 4902–4906.
- [6] Z. Tang, Y. Liu, M. He, W. Bu, Chemodynamic therapy: tumour micro-environment-mediated Fenton and Fenton-like reactions, *Angew. Chem. Int. Ed.* 58 (2019) 946–956.
- [7] S. Wang, Z. Wang, G. Yu, Z. Zhou, O. Jacobson, Y. Liu, Y. Ma, F. Zhang, Z. Chen, X. Chen, Tumor-specific drug release and reactive oxygen species generation for cancer chemo/chemodynamic combination therapy, *Adv. Sci.* 6 (2019) 1801986.
- [8] S.L. Richards, K.A. Wilkins, S.M. Swarbrick, A.A. Anderson, N. Habib, A.G. Smith, M. McAnish, J.M. Davies, The hydroxyl radical in plants: from seed to seed, *J. Exp. Bot.* 66 (2014) 37–46.
- [9] F. Shahidi, Y. Zhong, Lipid oxidation and improving the oxidative stability, *Chem. Soc. Rev.* 39 (2010) 4067–4079.
- [10] V. Sosa, T. Moliné, R. Somoza, R. Paciucci, H. Kondoh, M.E. LLeonart, Oxidative stress and cancer: an overview, *Ageing Res. Rev.* 12 (2013) 376–390.
- [11] M.G. Simic, D.S. Bergtold, L.R. Karam, Generation of oxy radicals in biosystems, *Mutat Res-Fund Mol M.* 214 (1989) 3–12.
- [12] Y. Nosaka, A.Y. Nosaka, Generation and detection of reactive oxygen species in photocatalysis, *Chem. Rev.* 117 (2017) 11302–11336.
- [13] G. Guan, X. Wang, B. Li, W. Zhang, Z. Cui, X. Lu, R. Zou, J. Hu, "Transformed" Fe_3S_4

- tetragonal nanosheets: a high-efficiency and body-clearable agent for magnetic resonance imaging guided photothermal and chemodynamic synergistic therapy, *Nanoscale* 10 (2018) 17902–17911.
- [14] M. Huo, L. Wang, Y. Chen, J. Shi, Tumor-selective catalytic nanomedicine by nanocatalyst delivery, *Nat. Commun.* 8 (2017) 357.
- [15] T. Yang, Y. Wang, H. Ke, Q. Wang, X. Lv, H. Wu, Y. Tang, X. Yang, C. Chen, Y. Zhao, Protein-Nanoreactor-assisted synthesis of semiconductor nanocrystals for efficient cancer theranostics, *Adv. Mater.* 28 (2016) 5923–5930.
- [16] Z. Li, J. Liu, Y. Hu, Z. Li, X. Fan, Y. Sun, F. Besenbacher, C. Chen, M. Yu, Biocompatible PEGylated bismuth nanocrystals: "All-in-one" theranostic agent with triple-modal imaging and efficient *in vivo* photothermal ablation of tumors, *Biomaterials* 141 (2017) 284–295.
- [17] S. Yang, Z. Li, Y. Wang, X. Fan, Z. Miao, Y. Hu, Z. Li, Y. Sun, F. Besenbacher, M. Yu, Multifunctional Bi@PPy-PEG core-shell nanohybrids for dual-modal imaging and photothermal therapy, *ACS Appl. Mater. Interfaces* 10 (2018) 1605–1615.
- [18] Y. Kai, L. Hu, X. Ma, S. Ye, C. Liang, X. Shi, C. Li, Y. Li, L. Zhuang, Multimodal imaging guided photothermal therapy using functionalized graphene nanosheets anchored with magnetic nanoparticles, *Adv. Mater.* 24 (2012) 1868–1872.
- [19] Z. Li, Y. Hu, K.A. Haward, T. Jiang, X. Fan, Z. Miao, Y. Sun, F. Besenbacher, M. Yu, Multifunctional bismuth selenide nanocomposites for antitumor thermo-chemotherapy and imaging, *ACS Nano* 10 (2015) 984–997.
- [20] M.C. Chen, Z.W. Lin, M.H. Ling, Near-infrared light-activatable microneedle system for treating superficial tumors by combination of chemotherapy and photothermal therapy, *ACS Nano* 10 (2015) 93–101.
- [21] Y. Zhang, R. Sha, L. Zhang, W. Zhang, P. Jin, W. Xu, J. Ding, J. Lin, J. Qian, G. Yao, Harnessing copper-palladium alloy tetrapod nanoparticle-induced pro-survival autophagy for optimized photothermal therapy of drug-resistant cancer, *Nat. Commun.* 9 (2018) 4236.
- [22] W. Fan, B. Yung, P. Huang, X. Chen, Nanotechnology for multimodal synergistic cancer therapy, *Chem. Rev.* 117 (2017) 13566–13638.
- [23] J. Kim, H.R. Cho, H. Jeon, D. Kim, C. Song, N. Lee, S.H. Choi, T. Hyeon, Continuous O₂-evolving MnFe₂O₄ nanoparticle-anchored mesoporous silica nanoparticles for efficient photodynamic therapy in hypoxic cancer, *J. Am. Chem. Soc.* 139 (2017) 10992–10995.
- [24] H. Zhu, Y. Wang, C. Chen, M. Ma, M. Gao, Monodisperse dual plasmonic Au@Cu_{2-x}E (E = S, Se) core@shell supraparticles: aqueous fabrication, multimodal imaging and tumor therapy at *in vivo* level, *ACS Nano* 11 (2017) 8273–8221.
- [25] Q. Huang, S. Zhang, H. Zhang, Y. Han, H. Liu, F. Ren, Q. Sun, Z. Li, M. Gao, Boosting the radiosensitizing and photothermal performance of Cu_{2-x}Se nanocrystals for synergistic radiophotothermal therapy of orthotopic breast cancer, *ACS Nano* 13 (2019) 1342–1353.
- [26] A. Kumar, R.P. Singh, T. Mohanty, A. Taneja, Tunable optical nonlinearity of Au-TiO₂ nanocomposites, *Photonics Nanostruct.* 33 (2019) 1–9.
- [27] Q. Tian, F. Jiang, R. Zou, Q. Liu, Z. Chen, M. Zhu, S. Yang, J. Wang, J. Hu, Cu₉S₅ nanocrystals: a photothermal agent with a 25.7% heat conversion efficiency for photothermal ablation of cancer cells *in vivo*, *ACS Nano* 5 (2011) 9761–9771.
- [28] Z. Wang, P. Huang, O. Jacobson, Z. Wang, Y. Liu, L. Lin, J. Lin, N. Lu, H. Zhang, R. Tian, G. Niu, G. Liu, X. Chen, Biomimetic-inspired synthesis of copper sulfide-ferritin nanocages as cancer theranostics, *ACS Nano* 22 (2016) 3453–3460.
- [29] C.M. Hessel, V.P. Pattani, M. Rasch, M.G. Panthani, B. Koo, J.W. Tunnell, B.A. Korgel, Copper selenide nanocrystals for photothermal therapy, *Nano Lett.* 11 (2011) 2560–2566.
- [30] L. Wang, J. Hou, S. Liu, A.J. Carrier, T. Guo, Q. Liang, D. Oakley, X. Zhang, CuO nanoparticles as haloperoxidase-mimics: chloride-accelerated heterogeneous Cu-Fenton chemistry for H₂O₂ and glucose sensing, *Sensor. Actuator. B Chem.* 287 (2019) 180–184.
- [31] T. Zheng, G.G. Li, F. Zhou, R. Wu, J. Zhu, H. Wang, Gold-nanosponge-based multistimuli-responsive drug vehicles for targeted chemo-photothermal therapy, *Adv. Mater.* 28 (2016) 8218–8226.
- [32] Y. Dou, Y. Guo, X. Li, X. Li, S. Wang, L. Wang, G. Lv, X. Zhang, H. Wang, X. Gong, J. Chang, Size-tuning ionization to optimize gold nanoparticles for simultaneous enhanced CT imaging and radiotherapy, *ACS Nano* 10 (2016) 2536–2548.
- [33] S. He, N.J.J. Johnson, V.A.N. Huu, E. Cory, Y. Huang, R.L. Sah, J.V. Jokerst, A. Almutairi, Simultaneous enhancement of photoluminescence, MRI Relaxivity, and CT contrast by tuning the interfacial layer of lanthanide heteroepitaxial nanoparticles, *Nano Lett.* 17 (2017) 4873–4880.
- [34] H. Zhang, T. Wang, W. Qiu, Y. Han, Q. Sun, J. Zeng, F. i Yan, H. Zheng, Z. Li, M. Gao, Monitoring the opening and recovery of the blood-brain barrier with noninvasive molecular imaging by biodegradable ultrasmall Cu_{2-x}Se nanoparticles, *Nano Lett.* 18 (2018) 4985–4992.
- [35] Y. Han, T. Wang, H. Liu, S. Zhang, H. Zhang, M. Li, Q. Sun, Z. Li, The release and detection of copper ions from ultrasmall theranostic Cu_{2-x}Se nanoparticles, *Nanoscale* 11 (2019) 11819–11829.
- [36] C. Hu, Z. Zhang, S. Liu, X. Liu, M. Pang, Monodispersed CuSe sensitized covalent organic framework photosensitizer with an enhanced photodynamic and photothermal effect for cancer therapy, *ACS Appl. Mater. Interfaces* 11 (2019) 23072–23082.
- [37] M.P. Rayman, Selenium in cancer prevention: a review of the evidence and mechanism of action, *Proc. Nutr. Soc.* 64 (2005) 527–542.
- [38] K.C. Grabar, R.G. Freeman, M.B. Hommer, M.J. Natan, Preparation and characterization of Au colloid monolayers, *Anal. Chem.* 67 (1995) 735–743.
- [39] Z. Li, Z. Li, L. Chen, Y. Hu, S. Hu, Z. Miao, Y. Sun, F. Besenbacher, M. Yu, c Polyethylene glycol-modified cobalt sulfide nanosheets for high-performance photothermal conversion and photoacoustic/magnetic resonance imaging, *Nano Research* 11 (2018) 2436–2449.
- [40] X. Sun, Y. Zou, J. Jiang, Surface plasmon resonances enhanced click chemistry through synergistic photothermal and hot electron effects, *Chem. Commun.* 55 (2019) 4813–4816.
- [41] J. Zeng, D. Goldfeld, Y.A. Xia, Plasmon-assisted optofluidic system for measuring the photothermal conversion efficiencies of gold nanostructures and controlling an electrical switch, *Angew. Chem. Int. Ed.* 52 (2013) 4169–4173.
- [42] Y. Cao, S. Li, C. Chen, D. Wang, T. Wu, H. Dong, X. Zhang, Rattle-type Au@Cu_{2-x}S hollow mesoporous nanocrystals with enhanced photothermal efficiency for intracellular oncogenic microRNA detection and chemo-photothermal therapy, *Biomaterials* 158 (2018) 23–33.
- [43] C.B. France, B.A. Parkinson, Physical and electronic structure of p-sexiphenyl on Au (111), *Appl. Phys. Lett.* 82 (2003) 1194–1196.
- [44] S. Navalon, R. Martin, M. Alvaro, H. Garcia, Gold on diamond nanoparticles as a highly efficient fenton catalyst, *Angew. Chem. Int. Ed.* 49 (2010) 8403–8407.
- [45] H. Li, S. Gan, H. Wang, D. Han, L. Niu, Intercorrelated superhybrid of AgBr supported on graphitic-C₃N₄-decorated nitrogen-doped graphene: high engineering photocatalytic activities for water purification and CO₂ reduction, *Adv. Mater.* 27 (2015) 6906–6913.
- [46] X. Hu, J. Tian, Y. Xue, Y. Li, H. Cui, Bi₂WO₆ Nanosheets decorated with Au nanorods for enhanced near-infrared photocatalytic properties based on surface plasmon resonance effects and wide-range near-infrared light harvesting, *ChemCatChem* 9 (2017) 1511–1516.
- [47] X. Wang, L. Ba, H. Liu, X. Yu, Y. Yin, C. Gao, A Unique disintegration-reassembly route to mesoporous titania nanocrystalline hollow spheres with enhanced photocatalytic activity, *Adv. Funct. Mater.* 28 (2018) 1704208.
- [48] Y. Yao, G. Wu, F. Lu, S. Wang, Y. Hu, J. Zhang, W. Huang, F. Wei, Enhanced photo-Fenton-like process over Z-scheme CoFe₂O₄/g-C₃N₄ Heterostructures under natural indoor light, *Environ. Sci. Pollut. Res. Int.* 23 (2016) 21833–21845.
- [49] D.E.J.G.J. Dolmans, D. Fukumura, R.K. Jain, Photodynamic therapy for cancer, *Nat. Rev. Canc.* 3 (2003) 380–387.
- [50] Z. Tang, H. Zhang, Y. Liu, D. Ni, H. Zhang, J. Zhang, Z. Yao, M. He, J. Shi, W. Bu, Antiferromagnetic pyrite as the tumor microenvironment-mediated nanoplatform for self-enhanced tumor imaging and therapy, *Adv. Mater.* 29 (2017) 1701683.
- [51] Z. Gan, X. Wu, M. Meng, X. Zhu, L. Yang, P.K. Chu, Photothermal contribution to enhanced photocatalytic performance of graphene-based nanocomposites, *ACS Nano* 8 (2014) 9304–9310.
- [52] X. Song, J. Xu, C. Liang, Y. Chao, Q. Jin, C. Wang, M. Chen, Z. Liu, Self-supplied tumor oxygenation through separated liposomal delivery of H₂O₂ and catalase for enhanced radio-immunotherapy of cancer, *Nano Lett.* 18 (2018) 6360–6368.
- [53] G. Song, Y. Chen, C. Liang, X. Yi, J. Liu, X. Sun, S. Shen, K. Yang, Z. Liu, Catalase-loaded TaOx nanoshells as bio-nanoreactors combining high-z element and enzyme delivery for enhancing radiotherapy, *Adv. Mater.* 28 (2016) 7143–7148.
- [54] Z. Ma, X. Jia, J. Bai, Y. Ruan, C. Wang, J. Li, M. Zhang, X. Jiang, MnO₂ Gatekeeper, An intelligent and O₂-evolving shell for preventing premature release of high cargo payload core, overcoming tumor hypoxia, and acidic H₂O₂-sensitive MRI, *Adv. Funct. Mater.* 27 (2017) 1604258.